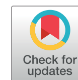

The crystal structure of human microsomal triglyceride transfer protein

Ekaterina I. Biterova[a,b], Michail N. Isupov[c], Ronan M. Keegan[d], Andrey A. Lebedev[d], Anil A. Sohail[a,b], Inam Liaqat[a], Heli I. Alanen[a,b], and Lloyd W. Ruddock[a,b,1]

[a]Faculty of Biochemistry and Molecular Medicine, University of Oulu, 90220 Oulu, Finland; [b]Biocenter Oulu, University of Oulu, 90014 Oulu, Finland; [c]Henry Wellcome Biocatalysis Centre, Biosciences, University of Exeter, EX4 4QD Exeter, United Kingdom; and [d]Research Complex at Harwell, Science and Technology Facilities Council Rutherford Appleton Laboratory, Didcot OX11 0FA, United Kingdom

Edited by Michael V. Airola, Stony Brook University, Stony Brook, NY, and accepted by Editorial Board Member Alan R. Fersht July 15, 2019 (received for review February 20, 2019)

Microsomal triglyceride transfer protein (MTP) plays an essential role in lipid metabolism, especially in the biogenesis of very low-density lipoproteins and chylomicrons via the transfer of neutral lipids and the assembly of apoB-containing lipoproteins. Our understanding of the molecular mechanisms of MTP has been hindered by a lack of structural information of this heterodimeric complex comprising an MTPα subunit and a protein disulfide isomerase (PDI) β-subunit. The structure of MTP presented here gives important insights into the potential mechanisms of action of this essential lipid transfer molecule, structure-based rationale for previously reported disease-causing mutations, and a means for rational drug design against cardiovascular disease and obesity. In contrast to the previously reported structure of lipovitellin, which has a funnel-like lipid-binding cavity, the lipid-binding site is encompassed in a β-sandwich formed by 2 β-sheets from the C-terminal domain of MTPα. The lipid-binding cavity of MTPα is large enough to accommodate a single lipid. PDI independently has a major role in oxidative protein folding in the endoplasmic reticulum. Comparison of the mechanism of MTPα binding by PDI with previously published structures gives insights into large protein substrate binding by PDI and suggests that the previous structures of human PDI represent the "substrate-bound" and "free" states rather than differences arising from redox state.

X-ray crystallography | abetolipoproteinemia | hypercholesterolemia | lipid metabolism | protein disulfide isomerase

The transport of the bulk of dietary and endogenous lipids is achieved by the assembly of chylomicrons and very low-density lipoproteins (VLDL; also called apolipoprotein B [apoB]-containing lipoproteins), which are produced in the intestine and liver, respectively (1–3). These large spherical particles contain apoB in addition to triglycerides (TGs), cholesteryl esters (CEs), phospholipids, and vitamins A and E. Current evidence suggests that the assembly of apoB-containing lipoproteins is a 2-step process occurring in the lumen of the endoplasmic reticulum (ER) (4). In the first step, a small amount of lipid is transferred to nascent apoB during translocation into the ER lumen, forming a primordial apoB particle. During the second step, lipid is added to the primordial apoB particle posttranslationally. The first step requires the ER-resident microsomal triglyceride transfer protein (MTP), which shuttles TG, CE, and phospholipids from the ER membrane to the primordial apoB particle (5). Without MTP function, underlipidated apoB is subjected to proteasomal degradation (6, 7). Defective or missing MTP function leads to abetalipoproteinemia (ABL; Online Mendelian Inheritance in Man database 200100), a rare autosomal recessive disorder (8–10). The disorder is characterized by a defect in assembly and secretion of hepatic and intestinal apoB-containing lipoproteins, VLDL, and chylomicrons, leading to fat malabsorption, subsequent steatorrhea, and fat-filled enterocytes and hepatocytes. Multiple point mutations within the *MTTP* gene resulting in ABL have been reported and characterized (11–18). MTP is the target for drugs to treat familial hypercholesterolemia in humans (19–21) and obesity in dogs (22).

MTP is a heterodimer consisting of a unique large MTP α-subunit (~97 kDa) and a multifunctional protein disulfide isomerase (PDI) β-subunit (~55 kDa) (23, 24). PDI is a ubiquitously expressed member of the thioredoxin superfamily, which catalyzes oxidation and isomerization of disulfide bonds during nascent protein folding (25). PDI comprises 4 thioredoxin-fold domains, of which 2 are catalytic, **a** and **a′**, and contain a characteristic CXXC catalytic motif (WCGHCK). The catalytic domains are separated by **b** and **b′** domains, with the **b′** domain providing the primary peptide binding site (26). The role of PDI in MTP function is uncertain beyond a role in maintaining MTPα in a soluble form (27) or ensuring that it remains in the ER through a C-terminal KDEL ER retrieval signal (5, 28).

MTP is a member of the large lipid transfer protein (LLTP) superfamily, which also includes apoB, apolipophorin I/II, and lipovitellin (29). Apolipophorin I/II, the major carrier of lipids in insects, and lipovitellin, which transports lipids to the developing oocyte in oviparous vertebrates and invertebrates, together with apoB function as vehicles for extracellular lipid transport. In contrast to other family members, MTP is not directly involved in

Significance

This study provides a structure for microsomal triglyceride transfer protein, a key protein in lipid metabolism and transport. Microsomal triglyceride transfer protein is linked to a human disease state, abetalipoproteinemia. The structure helps us to understand how this protein functions and gives a rationale for how previously reported mutations result in loss of function of the protein and hence, cause disease. The structure also provides a means for rational drug design to treat cardiovascular disease, hypercholesterolemia, and obesity. Microsomal triglyceride transfer protein is composed of 2 subunits. The β-subunit, protein disulfide isomerase (PDI), also acts independently as a protein folding catalyst. The structure that we present here gives insights into how PDI functions in protein folding.

Author contributions: L.W.R. designed research; E.I.B., A.A.S., I.L., H.I.A., and L.W.R. performed research; E.I.B., M.N.I., R.M.K., A.A.L., A.A.S., and I.L. analyzed data; and E.I.B. and L.W.R. wrote the paper.

Conflict of interest statement: A patent for the production system used to make the protein for structural studies using sulfhydryl oxidases in the cytoplasm of *Escherichia coli* is held by the University of Oulu: Method for producing natively folded proteins in a prokaryotic host (patent no. 9238817; date of patent January 19, 2016; inventor: L.W.R.).

This article is a PNAS Direct Submission. M.V.A. is a guest editor invited by the Editorial Board.

This open access article is distributed under Creative Commons Attribution-NonCommercial-NoDerivatives License 4.0 (CC BY-NC-ND).

Data deposition: The data have been deposited in the Protein Data Bank, www.wwpdb.org (PDB ID code 6I7S).

[1]To whom correspondence may be addressed. Email: lloyd.ruddock@oulu.fi.

This article contains supporting information online at www.pnas.org/lookup/suppl/doi:10.1073/pnas.1903029116/-/DCSupplemental.

lipid transport to distant tissues and is not secreted. Evidence suggests that MTP may be the oldest member of the LLTP superfamily, which has given rise to paralogous family members, including apoB (30).

Members of the LLTP superfamily share significant sequence homology and a conserved N-terminal module consisting of a β-barrel and an α-helical domain (30, 31). The C-terminal lipid-binding domain has diverged among LLTP family members, reflecting their abilities to bind different types and quantities of lipid. Based on sequence and domain architecture similarity, MTP, the smallest member of the family, has been predicted to consist of 3 domains: an N-terminal β-barrel domain, a central α-helical domain, and a C-terminal 2 β-sheet domain. A large body of published evidence has suggested separate functions for the domains. MTP acts as a chaperone and stabilizes the nascent apoB molecule via interactions with the β-barrel and central helical domains (32, 33). The central α-helical domain is reported to also act as the binding site for PDI (32). Lipid-binding and transfer activity occurs in the C-terminal domain, with a strong preference toward neutral 3 chain-containing lipids (34).

Among all LLTP members, only the crystal structure of lamprey lipovitellin has been reported to date (35–37). This structure provided an essential structural basis for understanding lipid binding and transfer by this class of proteins. However, the wide divergence in the lipid-binding domains in the superfamily hinders understanding of the molecular mechanisms of action of other families. Here, we describe the crystal structure of the heterodimer of human MTP at 2.5-Å resolution. The structure reveals the lipid-binding site in MTP, gives a rationale for disease-causing mutations, and gives insights on the molecular mechanisms of PDI interaction with large protein substrates. Given the ability of MTP to modulate the concentration of apoB-containing lipoproteins in blood plasma, the crystal structure also provides the means for the rational drug design against obesity and cardiovascular disease.

Results and Discussion

Overall Structure of MTP–PDI Protein Complex. To provide a structural basis to facilitate the understanding of the mechanisms of action of lipid transfer by MTP, we determined the crystal structure of the full-length heterodimeric protein complex to 2.5 Å (structure quality is in *SI Appendix*). Overall, the MTP complex adopts a large extended cradle-like structure measuring ∼130 Å in the longest direction and ∼80 Å in the shortest, and it contains ∼2,100 $Å^2$ of buried area at the interface between the 2 subunits. As reported previously and as evident from the crystal structure, MTPα comprises 3 distinctive domains (Fig. 1): 1) an N-terminal half β-barrel (amino acids 21 to 297), suggested to be involved in interactions with apoB (32); 2) an α-helical domain (amino acids 298 to 603), previously proposed to be implicated in interaction with PDI and apoB (32, 33); and 3) a C-terminal domain (amino acids 604 to 884), which encompasses the lipid-binding site sandwiched between 2 β-sheets named the A- and C-sheets.

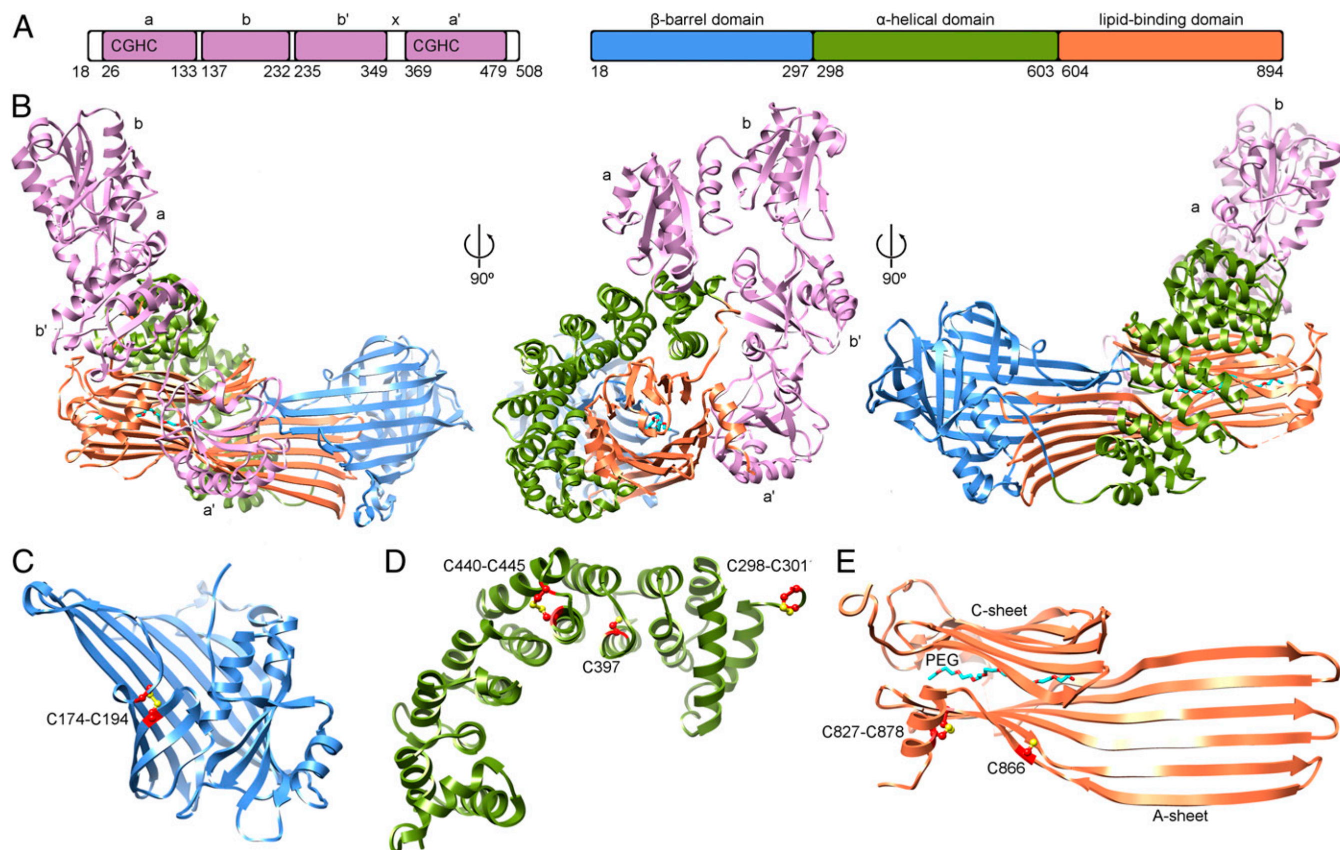

Fig. 1. Structure of MTP. (*A*) Domain architecture of PDI (*Left*) and MTP (*Right*). The Cys-Gly-His-Cys active site motifs of PDI are indicated. (*B*) Ribbon representation of the MTPα–PDI complex structure. The 3 views are related by a 90° rotation around a vertical axis. The complex is colored according to *A*. The missing region (MTPα amino acids 717 to 721) is shown by broken lines. Bound PEG is shown in stick representation in cyan. (*C*–*E*) Ribbon representation of the β-barrel domain (*C*), α-helical domain (*D*), and lipid-binding domain (*E*). Cysteine residues are shown in ball and stick representation and colored in red. The N-terminal β-barrel domain has a gap between strands β5 and β6, allowing a few residues (Asn147 and Arg150) of the central α-helix to be exposed and form hydrogen bonds with the coil connecting the β-barrel and α-helical domains. In the α-helical domain, 3 layers of side chains are formed by the 2-layer arrangement of the α-helices. There is a large buried surface between 2 layers of helices formed by hydrophobic residues and an additional surface formed between the helical domain and the β-sheets of the C-terminal domain. The outer surface contains more polar and ionizable side chains.

In a structure similar to that of lipovitellin (*SI Appendix*, Fig. S1*A*), the N-terminal β-barrel consists of 3 short α-helices and 13 β-strands, which surround the fourth longer α-helix (Fig. 1*C*). The β-barrel is not a continuous structure, having one side being formed by shorter β-strands. The unusual shape of the β-barrel domain results in the formation of a pit that, similar to lipovitellin, accommodates the β-strand segments and loops of the A-sheet of the C-terminal domain (*SI Appendix*, Fig. S1 *A* and *C*). The longer side of the β-barrel forms a slightly twisted β-sandwich with 3 strands of the A-sheet and is predominantly stabilized by hydrophobic interactions. Previous publications refer to this region as a flexible "ball-and-socket" junction, which might accommodate lipid (36, 37). In contrast to lipovitellin, the N-terminal β-barrel domain contains only 1 disulfide bond between Cys174 and Cys194. This is conserved in lipovitellin (Cys156 to Cys182) and apoB (Cys186 to Cys212), and it braces together a coiled region between strands β7 and β8 with strand β7 (Fig. 1*C*). The second pair of cysteines forming a disulfide bond, Cys289 and Cys301, is located in the long coiled segment connecting the N-terminal β-barrel and the middle α-helical domain (Fig. 1*D* and *SI Appendix*, Fig. S1 *B* and *C*). This disulfide is not present in lipovitellin or apoB.

The α-helical domain of MTPα is similar to that of lipovitellin (*SI Appendix*, Fig. S1*B*) and forms a superhelical right-handed coiled-coil with a 2-helix repeating unit (Fig. 1*D*). The domain encompasses 2 layers of 17 helices and 1 3_{10}-helix forming a clamp, which holds together one side of the C-sheet and A-sheet of the C-terminal lipid-binding cavity and encloses it from the solvent. From the other side, the C-terminal domain is braced by extensive interactions between the **a**′ domain of PDI and MTPα. A region between helices α8 and α9 is stabilized by a disulfide bond between Cys440 and Cys445 (Fig. 1*D*) in a position equivalent to that found in lipovitellin (Cys443 to Cys449). This disulfide is not conserved in apoB and is not conserved in the MTP family (see below). One unpaired, nonconserved Cys397 is buried within the hydrophobic core of the domain.

The C-terminal domain of MTP is formed by 2 β-sheets, which according to convention, are named the A- and C-sheets. The A- and C-sheets form a slightly twisted sandwich (Fig. 1*E*), which encompasses the lipid-binding site between them. This is in stark contrast with the funnel-like structure found in lipovitellin (*SI Appendix*, Fig. S1*C*). The narrow lipid-binding cavity of MTP reflects its ability to bind only a limited amount of neutral lipid at a time—as has been previously suggested by biochemical evidence (38). The C-sheet is formed from 6 antiparallel β-strands, which line the C-terminal part of the α-helical domain. The A-sheet is also formed from 6 antiparallel β-strands, which are twice as long as than those of the C-sheet. One-half of the A-sheet forms a lipid-binding site with C-sheet (see below), and the other half interacts with the N-terminal β-barrel domain. There are few interactions between the A- and C-sheets, and these mostly occur on the edges of the β-sandwich, blocking access to the lipid-binding site from solvent.

There is an 11-amino acid α-helix at the end of the C-terminal domain. It is positioned at ~90° relative to strand β5 of the A-sheet and is stabilized in this conformation by 2 hydrogen bonds between the side chain of Asn874 and the backbone of Met828 and by a disulfide bond between Cys827 and Cys878 (Fig. 1*E*). This disulfide is important for the tertiary structure of MTP and its function—mutation of Cys878 to Ser results in lower expression and loss of lipid-transferring activity (11). An unpaired, nonconserved, Cys866 located in strand β6 faces the lipid-binding site.

PDI in the complex adopts the horseshoe shape seen previously (39, 40), and all 4 domains (**a**, **b**, **b**′, and **a**′) are clearly defined in our heterodimer structure (Fig. 1*B*). MTPα interacts with PDI via its α-helical and C-terminal domains.

Interactions with PDI. MTPα interaction with PDI is obligatory, and disruption of the heterodimer leads to the loss of the lipid transfer activities and aggregation of the large MTPα subunit (27). Experimental evidence and the crystal structure presented here both indicate that the association of PDI and MTP is predominantly hydrophobic. PDI interacts with MTPα via 3 of its 4 domains: **a**, **a**′, and **b**′ (Figs. 1*B* and 2*A*). Comparison of interactions formed by the **a**, **a**′, and **b**′ domains of PDI reveals that the **b**′ domain provides a primary binding site for MTP, consistent with previous biochemical evidence that it provides the primary binding site for other protein substrates (26).

MTPα interacts with the **b**′ domain of PDI via the C-terminal half of helix α17 of the helical domain and the loop (amino acids 594 to 610) on the border between the α-helical domain and C-sheet. This loop protrudes from the surface of MTP and interacts with a hydrophobic pocket in the **b**′ domain (Fig. 2 *B* and *C*). Tyr605 of MTPα plays a major role in this interaction and creates multiple contacts with residues lining the binding pocket of PDI. The interaction of Tyr605 of MTPα with PDI is supported by several hydrogen bonds formed by neighboring residues and by the side chain of Met600 binding in a spatially adjacent hydrophobic pocket. Asn604 seems to play a critical role in fixing the conformation of this loop as its side chain forms hydrogen bonds with the backbone of Met600, Asp606, and Arg607. Asn604 and Tyr605 are conserved in MTPα.

The **a** and **a**′ catalytic domains of PDI use equivalent surfaces to interact with MTPα, with the catalytic CGHC motifs buried at the interface. The active site cysteines in both catalytic domains of PDI are in the reduced state, and the surface-exposed N-terminal catalytic cysteines are located within 4 Å of MTPα (Fig. 2 *D* and *E*). The **a** domain interacts with side chains of helices α13 and α15 of the α-helical domain (Fig. 2*D*). The **a**′ domain makes contacts with residues in the lipid-binding domain, including strands β5 and β6 of the A-sheet, β1 of the C-sheet, and the C-terminal α-helix (Fig. 2*E*).

Lipid-Binding Site of MTP. The primary function of MTP is the transfer of lipids for the assembly and secretion of VLDLs by the liver and chylomicrons by the intestine (5). The lipid-binding pocket of MTP has been suggested to be hydrophobic in nature based on the distinctive preference of MTP toward neutral lipids compared with charged lipids (34). However, it is capable of binding and transferring a wide variety of lipid molecules, suggesting either promiscuity of binding or the presence of multiple lipid-binding sites.

In the MTP crystal structure, there is a molecule of polyethylene glycol (PEG) bound between β-sheets A and C, and this probably occupies the lipid-binding site—with the PEG molecule being considered as a lipid mimic (Fig. 3 and *SI Appendix*, Fig. S2). PEG is bound in both MTPα chains of the asymmetric unit in different conformations, reflecting the flexibility of lipid binding. When compared with lipovitellin (*SI Appendix*, Fig. S1*C*), the lipid-binding pocket of MTP is not a funnel-like structure, but instead, it is a confined space. The calculated volume of the cavity is ∼2,100 $Å^3$ (41), comparable with the volume of a single triacylglyceride molecule (∼1,620 $Å^3$ for triolein). This is in agreement with previous biochemical evidence that the lipid-binding site can accommodate only a small number of lipid molecules with a maximal number of observed bound triolein of less than 1 per MTP (38). One of the bound PEGs (cyan in Fig. 3) interacts along the entire length of the lipid-binding pocket and runs parallel to the A-sheet between strands β3 and β4 and between strands β2 and β4 and across β3 of the C-sheet (Fig. 3 *B* and *C*). The second bound PEG molecule (green in Fig. 3) interacts closer to the "pivot" formed by the C-sheet and the N-terminal domain; starting from the middle between strands β3 and β4 of the A-sheet, it takes a turn across strand β4 and extends a small tail between strands β4 and β5.

Electrostatic surface analysis of the inner interfaces of A- and C-sheets indicates the presence of a predominantly neutral surface (*SI Appendix*, Fig. S2*A*), which would favor binding of neutral lipid moieties, such as TGs. No distinctive charged patches are visible on the inner interface of the lipid-binding pocket, which could bind charged head groups of phospholipids or phosphatidylcholines. Previous studies showing that MTP is capable of binding and transferring a wide class of lipids, including phospholipids, from the ER membrane suggested the presence of a second "slow" binding site in MTP (34, 38). It is

BIOCHEMISTRY

Fig. 2. Interactions between PDI and MTPα. (*A*) Interactions between MTPα (*Left*) and PDI (*Right*) are shown in surface representation in yellow (**a** domain of PDI and α13 and α15 helices of the α-helical domain of MTPα), pink (**b**′ domain of PDI binding mainly to the helix α17 and the loop connecting the α-helical domain to the C-terminal domain of MTPα), and green (**a**′ domain of PDI interacting with β1-strand of C-sheet, β5- and β6-strands of A-sheet of MTPα, and 11-amino acid C-terminal α-helix). The C-terminal α-helix is indicated with C. To expose the interacting surfaces, PDI was pulled away from MTPα and rotated 180° around a vertical axis and 90° around the *z* axis. (*B*) Close-up view at the interaction of MTPα with the **b**′ domain of PDI. (*C*) The view is related to *B* by ∼180° rotation around the *y* axis and depicts a hydrophobic surface representation of the **b**′ domain of PDI with the hydrophobic residues colored in tan. The interacting loop of MTPα makes 2 turns and inserts the side chains of Met600 and Tyr605 into hydrophobic pockets of the **b**′ domain. (*D* and *E*) Close-up views at interactions of MTPα with the **a** (*D*) and **a**′ (*E*) domains of PDI. Interacting residues are shown in stick representation and colored according to Fig. 1. Cysteine residues of both protein molecules are shown in ball and stick representation. Cysteines of the active site motifs (Cys_{53}-Gly_{54}-His_{55}-Cys_{56} and Cys_{397}-Gly_{398}-His_{399}-Cys_{400}) of PDI are in the reduced state. Cys827 and Cys878 of MTPα form a disulfide bond. Hydrogen bonds are shown in dashed black lines.

Fig. 3. Lipid-binding site of MTPα. (*A*) The lipid-binding site is formed by a sandwich between the A- and C-sheets (surface representation). (*B* and *C*) Close-up view of the lipid-binding site of the C-sheet (*B*) and A-sheet (*C*) with PEG molecules bound (depicted in cyan color from chain H and green color from chain G). The lipid-binding site is formed mostly from hydrophobic residue side chains. The side chains of Phe767, Thr776, Val778, Asn780, Phe813, Ser815, Val817, and Phe819 of the A-sheet and Leu633, Ile642, Leu643, Ser646, Leu648, Ile650, Ser662, Val664, Ile666, and Leu696 of the C-sheet are within 4.5 Å of the PEG molecule from chain H. PEG from chain G is placed within 4.5-Å distance from side chains of Val778, Asn780, Ala809, Leu811, and Phe813 of the A-sheet and Ile621, Leu633, Ser646, Leu648, Ile650, Gly661, Ser662, Val664, Ile666, and Leu696 of the C-sheet.

not possible to confirm such an additional site on the current structure, but it could be speculated that a conformational change in MTP may result in a second lipid-binding site at the interface sandwiched between the A-sheet and the N-terminal β-barrel domain. This region contains some positively charged side chains, which may interact with charged phosphoryl groups.

To confirm the correct identification of the lipid-binding site, 7 mutations were made in the cavity (L633F, S662L, V664F, V664H, V664Y, V778L, and F813H). The V664H mutant caused strong growth defects even uninduced, and the V664Y mutant was produced in low yields; therefore, they were not studied further. Mutations L633F and F813H showed significantly reduced lipid transfer activity, while S662L, V664F, and V778L showed higher activity than the wild-type enzyme (*SI Appendix*, Fig. S3*B*). The mutations with the greatest effect on activity, V664F and F813H, were purified on a larger scale to confirm that the change in activity did not result from altered folding and/or instability (*SI Appendix*, Fig. S3 *C*, *D*, and *F*).

Mutations Causing ABL. Understanding of the role of MTP in apoB transfer and assembly in part emerged from the discovery of mutations in MTPα that cause ABL (42–44). To date, at least 18 natural missense variants of the *MTTP* gene have been reported, with 10 of these being reported to cause ABL. In addition, a number of frameshift, nonsense, and splice-site mutations leading to a complete loss of MTP have been reported (11, 12, 43–49). No mutations in the gene for PDI have been reported to cause ABL. This is consistent with the interaction site between them being the same as that used by PDI for substrate proteins, and hence, any mutations in PDI, which could lead to ABL, would instead be lethal. Several missense mutations in *MTTP* known to cause ABL have been extensively studied in vitro in an attempt to gain insights into the role of each of 3 MTPα domains in PDI binding and lipid transfer activity (15–18, 50, 51). Based on the crystal structure, more insights can be made into these mutations.

The reported mutations can be broadly grouped into 2 categories: those that abolish binding to PDI and transfer of lipids and those that retain the ability to bind to PDI but abolish lipid transfer (Fig. 4). The former group includes D169V (16), D361Y (17), R540C (15), R540H (12), and a 30-amino acid truncation from the C terminus (18). From the crystal structure, all 4 point mutations might be predicted to either result in misfolding or significantly destabilize the native state by disrupting salt bridges (D169V, D361Y) or hydrogen bonding (D169V, D361Y, R540C, R540H). In addition, Arg540 is located in close proximity to the **a** domain of PDI; hence, its mutation may have a direct negative impact on PDI association. The 30-amino acid truncation of MTP from the C terminus will nearly completely eliminate the interaction site with the **a**′ domain of PDI.

Mutations that have been reported to retain the ability to bind PDI but abolish lipid transfer include L435H (14), Y528H (15), and S590I (51) in the helical domain and N649S (15), G746E (51), and N780Y (51) in the lipid-binding domain. Of these 6 amino acids, only Asn780 faces the lipid-binding site directly. Hence, the N780Y mutation may directly affect lipid binding. The other 5 mutations probably affect lipid transfer activity indirectly by inducing conformational change and/or destabilizing the structure through the loss of structure-stabilizing hydrogen bonds (Y528H, S590I, N649S), the disruption of a hydrophobic interface (L435H), or the exposure of a hydrophobic side chain (S590I). Of the 6 amino acids, only Gly746 is conserved. Gly746

Fig. 4. Mapping of ABL-causing mutations to the MTP crystal structure. Residues, the mutations of which are reported to abolish lipid transfer but retain the ability to bind PDI, are shown in orange balls. Residues, the mutations of which are reported to abolish the binding of PDI and transfer of lipids, are indicated by blue balls. The C-terminal 30-amino acids truncation of MTP is also shown in blue.

forms part of the tight turn between β-strands β1 and β2 of A-sheet and has φ/ψ values that are not permitted to other amino acids. The G764E mutation is likely to severely disrupt the interactions between the A-sheet and the β-barrel domain.

To confirm this structural analysis, 9 missense mutations in *MTTP* that cause ABL were made. Seven of these (D169V, L435H, Y528H, R540C, R540H, G764E, and N780Y) could not be produced in our system or were produced in yields too low to analyze (<5% of wild-type protein). Hence, most of the mutations seem to cause folding and/or stability defects consistent with the prior literature and our structure-based analysis. Two mutants (S590I and N649S) could be made in higher yields but were still ∼3 to 4 times lower than that of the wild-type protein. Both show decreased lipid transfer activity but CD spectra and thermal denaturation curves equivalent to the wild-type protein (*SI Appendix*, Fig. S4). Hence, these mutations seem to affect both folding efficiency and lipid transfer activity.

Bioinformatics Analysis of MTP from Different Species. MTP is suggested to be the oldest member of the LLTP superfamily (30) and as such, can be found in a wide range of eukaryotic species. Studies on the evolution of MTP have suggested the coemergence of triacylglycerol transfer activity of MTP and apoB (52) such that mammals, birds, and fish (and other vertebrates) have TG transfer activity and possess apoB, while insects lack both. However, *Drosophila* MTP can support secretion of human apoB (53), suggesting overlapping conservation of function.

Since residues involved in function are usually conserved, we undertook structure-based conservation analysis to determine critical residues for MTP function. A dataset of 300 MTP sequences from different organisms was split into subsets containing 216 vertebrate sequences, 156 mammalian + bird sequences, and 94 mammalian sequences. Generally, conservation in the mammalian subset was too high to yield useful information, but it supported the conclusions drawn from the other sets. Conservation of amino acids in each of the sets was then mapped back onto the primary (*SI Appendix*, Fig. S5) or tertiary structure (Fig. 5*A*) of human MTP. Since the larger dataset is more likely to contain DNA sequence errors, the conservation threshold for this was chosen to be 98%. In each dataset examined, conservation in the lipid-binding domain was higher than in either of the other domains (Table 1).

Within the β-barrel, conservation was limited (conservation 3.6%; 8.9% within the vertebrate subset). Apart from Trp69 and Gly130, which were conserved in all datasets, conservation was located predominantly in the long central α-helix and the following 2 β-strands (β6 and β7) (*SI Appendix*, Figs. S5 and S6). None of the conserved residues—even within the more homologous mammalian + bird data subset (22.5% conservation)—were on the surface of the protein (Fig. 5*B*), raising questions regarding the proposed interaction between this domain and apoB. Even within the highly conserved mammalian subset (34.6% conservation), the majority of conserved residues in the β-barrel domain were buried, and the only surface-exposed patch of conserved amino acids was centered on the N-terminal region before β1, the farthest point in MTP from the lipid-binding site.

Within the α-helical region, conservation was higher than that for the β-barrel within all datasets (Table 1), but still, the solvent exposure of the conserved residues was minimal. Within the vertebrate subset, no linear stretches of amino acids showed high conservation (*SI Appendix*, Fig. S6). While the C terminus of α6 ending in Cys397 showed high conservation in the mammalian + bird subset (Fig. 5*A* and *SI Appendix*, Fig. S6), all of these residues are buried in the core of the protein. In all sets (*SI Appendix*, Fig. S5) residues interacting with the tip of the C-sheet were conserved, including Asn479, Glu570, and Asp361, which all form structure-stabilizing hydrogen bonds. Two of the residues within 5 Å of the **a** domain of PDI are conserved in the vertebrate subset, Gln530 and Arg540, with Arg540 conserved in every MTP sequence examined. It is unclear what the function of these 2 residues is, but mutations in Arg540 are reported to cause ABL (12, 15). The closest residues in PDI to the side chain of either are Pro51 or Trp52, but the closest distance is nearly 5 Å, while the side chains of Gln530 and Arg540 are within 3.4 Å of each other.

The conservation within the lipid-binding domain was the highest (Table 1 and *SI Appendix*, Figs. S5 and S6); despite virtually no conservation in the region of the A-sheet in contact with β-barrel, 2 of 68 amino acids in the vertebrate subset are conserved.

Fig. 5. Structure-based analysis. Structure-based conservation analysis of MTPα from the full (300 sequences; dark red), vertebrate (216 sequences; dark red and orange), and mammalian + bird (156 sequences; dark red, orange, and yellow) data subsets. Residues N147, Q358, T368, P552, Y574, L743, G763, L769, and L870 are conserved in 300 (98%) and mammalian + bird sets but not in the vertebrate sets, and the residues A374, A690, G746, and G755 are conserved only within the 300 (98%) subset. (*A*) Conserved residues from 3 subsets are mapped on the MTPα structure. Conservation is limited within the β-barrel and α-helical domains and mostly clustered in the lipid-binding segment of the C-terminal domain. PDI is shown in pink. Conserved residues mentioned in the text are indicated. (*B*) MTPα structure is shown in surface representation in 3 different views identical to those in Fig. 1*B*, indicating that there are no apparent conserved surface-exposed patches except for the middle view face of the lipid-binding site. (*C*) Ribbon representation of the lipid-binding domain with conserved residues from all 3 subsets shown. The conservation is poor in the sites of interaction of A-sheet with the β-barrel and within the lipid-binding site. (*D*) Close-up view of the middle orientation from *B* showing regions of conserved residues that might be involved in interactions with apoB. The majority of conserved residues are surface exposed and located in the loops connecting β-strands and 2 sheets (amino acids 702 to 714 and 768 to 770).

Table 1. Conservation of amino acids in MTPα

Source	β-Barrel domain, %	α-Helical domain, %	Lipid-binding domain, %
All species (300)	3.6	4.6	8.6
Vertebrate (216)	8.9	8.2	18.2
Mammalian + bird (156)	22.5	28.4	38.4
Mammalian (94)	34.6	45.1	52.2

For the vertebrate, mammalian + bird, and mammal datasets, conservation is set at 100%; for the larger dataset, which may contain a higher proportion of DNA sequencing errors, it is set at 98%.

Excluding this part, vertebrate conservation in the lipid-binding region is 23.0%, more than 2.5-fold higher than in either of the other domains, suggesting functional importance. The expected high conservation in the lipid-binding site, however, is not visible (Fig. 5*C*). Only 4 of 23 amino acids within 4.5 Å of the bound PEG are conserved among vertebrates, while in the mammalian + bird dataset, only 9 of 23 are conserved. Instead of conserved amino acids, the lipid-binding site contains similar—predominantly hydrophobic—amino acids. This similarity, rather than conservation, is consistent with MTPs capability to bind and transfer a wide variety of lipid molecules. This is also consistent with the inability to produce mutants that introduce less hydrophobic residues in these sites V664H, V664Y, and N780Y, while making hydrophobic substitutions (S662L, V664F, V778L) did not inhibit MTP lipid transfer activity.

The lipid-binding domain forms interactions with the **b**′ and **a**′ domains of PDI. Of the 26 amino acids of this domain within 4.5 Å of PDI, 7 are conserved among vertebrates, and 3 of these are also conserved in the 300 (98%) set (Fig. 5*D*). These 3 are Asn604 and Tyr605, which make intimate contact with the **b**′ domain of PDI, as well as Cys878, which forms a disulfide bond with Cys827 near the **a**′ domain. The highest conservation in the lipid-binding domain is neither at the lipid-binding site nor near the PDI interaction site (Fig. 5*D* and *SI Appendix*, Fig. S6). Instead, 67% of the amino acids in the region Arg702 to Lys716 are conserved in the vertebrate subset. Leu713 and Met714 along with Ser768 to Trp770 form a conserved surface-exposed patch, which is extended in to a cleft between the lipid-binding domain and the helical domain by Phe706 and Phe707. These regions act as loops linking the β-strands that form the lipid-binding cavity. As these are the only conserved surface-exposed residues, it is tempting to speculate that this conserved surface-exposed patch may form an interaction site for another protein (e.g., the binding site for apoB) and that binding may allow egress of the lipid from the spatially adjacent binding site. However, this hypothesis should be experimentally verified.

Conformation of PDI Bound to Large Protein Substrates. Despite extensive research, so far the mechanistic detail of how PDI interacts with large protein substrates during catalysis of native disulfide bond formation has not been elucidated. It has been shown that PDI requires the **a** or **a**′ domains in combination with **b**′ to perform oxidation and isomerization function (25) and that the **b**′ domain provides the primary binding site while other domains also contribute to binding (26). To date, there is only 1 reported structure of PDI in complex with a "substrate" molecule, and that was using PDI from the soft rot fungus *Humicola insolens* (54). No specificity for substrate binding by any of the substrate binding sites in PDI has previously been reported, but the specificity of the substrate binding site in the **b**′ domain of PDIp (pancreas-specific PDI) has been reported to be a single aromatic amino acid with no adjacent negative charge in the substrate (55). This is consistent with the location of the side chain of Tyr605 of MTPα in a hydrophobic pocket in PDI. It is also consistent with the reported inhibition of PDI by small aromatic molecules, such as bisphenol (56). Determination of the MTP crystal structure not only gives information of the potential role of PDI in the complex but also, provides essential insight into PDI interactions with large proteins, i.e., MTPα may be considered to be a substrate mimic.

The structure of PDI in the MTP complex is significantly different from that previously obtained for human full-length PDI alone (39). While the 4 thioredoxin domains exhibit the same structures (rmsd 0.42 to 0.78 Å for the individual domains compared with reduced PDI; 4EKZ), the orientation of these domains with respect to each other changes, with movement of the **a**′ domain being the most pronounced change (Fig. 6). Comparison of the 2 catalytic motifs in PDI from MTP complex with reduced PDI (4EKZ) showed that binding to MTPα does not distort their geometry.

Conformational exchange in PDI has been reported before and has been linked both to the substrate bind–release cycle (57) and to conformational exchange linked to changes in the thiol-disulfide status of the active sites (58). The 2 previously available crystal structures of human PDI have been reported to represent the oxidized (4EL1) and reduced (4EKZ) states of the protein, with the major change being the orientation of the domains with respect to each other (39). This conformational change linked to changes in redox structure has been potentially linked to function (59), more specifically to modulating substrate binding. However, it should be noted that PDI acts to catalyze both the introduction of disulfide

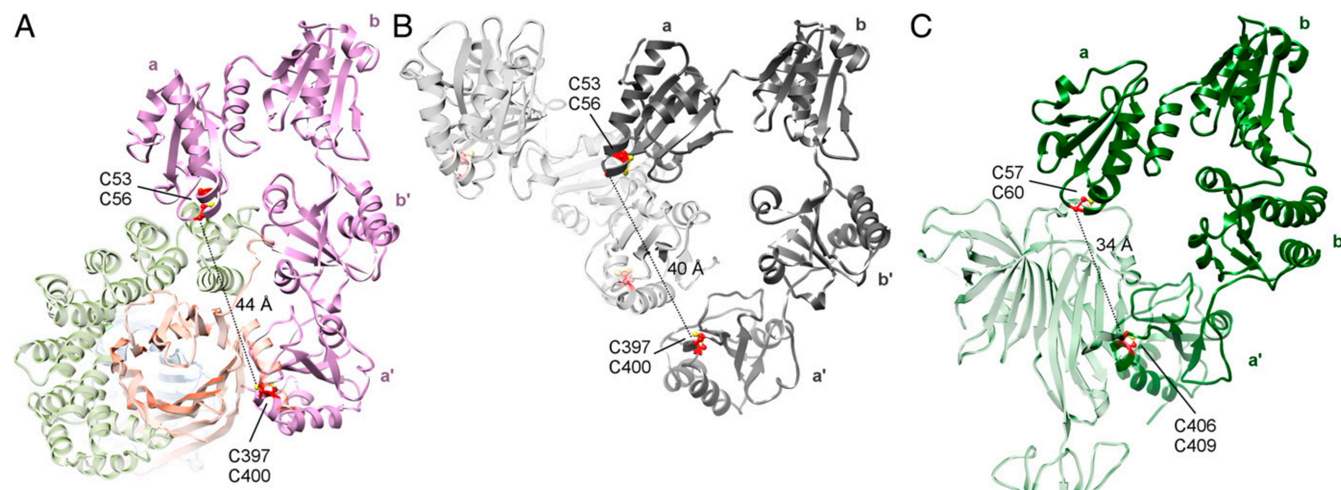

Fig. 6. Insights on PDI bound to protein substrates. Comparison of PDI conformations in MTP complex (*A*), oxidized PDI homodimer complex (*B*; 4EL1), and the PDI family member ERp57 in complex with Tapasin (*C*; 3F8U). All 3 molecules were superimposed and are shown in a similar orientation. Active site cysteines are colored in red and shown in ball and stick representation.

bonds in folding protein substrate from its oxidized state and the isomerization of disulfide bonds from its reduced state, and hence, both states must bind to nonnative protein substrates (60). In silico analysis suggests that interconversion between the 2 states is possible through domain motion independent of redox state (61). In the MTP complex structure, both active sites of PDI are in the reduced state, but the PDI is not in the "closed" conformation previously associated with this state; rather, it is in an "open" conformation with MTPα in the central cavity (Fig. 6). The interaction sites between PDI and MTPα are juxtaposed to the active sites in the **a** and **a′** domain and involve the previously identified "primary substrate binding site" in the **b′** domain (26). As such, the bound MTPα most probably mimics a large substrate protein bound to PDI. The more open conformation of PDI in the complex reflects the conformational flexibility of PDI for binding substrates of different sizes.

Several crystal structures of PDI family members have dimers of PDI in the asymmetric unit or form dimers with symmetry molecule. These include the first published structure of a PDI, yeast Pdi1p (40) (2B5E), and the structure of oxidized human PDI (39) (4EL1). In both of these structures, 1 domain of the other molecule of PDI sits in the cleft formed between the **a**, **b′**, and **a′** domains—just as MTPα sits in the cleft in our complex crystal structure. For oxidized human PDI, the interaction sites on the **a** and **a′** domains of the binding molecule mirror those used by PDI to bind MTPα (Fig. 6 and *SI Appendix*, Fig. S7). In the 4EL1 homodimer structure, the bound PDI does not formally contact the **b′** domain of the binding molecule. However, 20 amino acids at the N terminus of the protein along with regions G250 to K254 and L320 to E323, which are involved in MTPα interaction, are missing from the structure, and the pocket between the bound and binding molecule is sufficiently large to accommodate all of the missing regions. This conservation of binding sites along with the requirement for PDI to bind substrate proteins of different sizes in both its oxidized and reduced states (60, 62–64) suggests that, in the 4EL1 structure, 1 molecule of PDI is bound as a substrate would be by the other PDI molecule. Hence, the different structures previously available for human PDI probably represent the substrate bound and free states rather than representing differences in redox state per se. A similar pattern of self-association can be observed in the Pdi1p structure (40).

No structures exist for human PDI binding to other peptide or protein substrates, but the peptide binding site in human PDI **b′** domain has been mapped by NMR (65, 66), and 1 crystal structure exists for *H. insolens* PDI **b′** to **a′** binding to an 11-amino acid peptide derived from the cytoplasmic protein α-synuclein. The interaction site localized to the **b′** domain in both types of study is at an equivalent site to that seen for MTPα interaction in our complex (*SI Appendix*, Fig. S8).

Finally, a heterodimeric complex between the PDI family member ERp57 and Tapasin has been published (67) (3F8U). As per MTP, the Tapasin sits in a cleft formed between the **a** and **a′** domains of ERp57, but in this case, Tapasin is insufficiently large to make contact with the **b′** domain. The interaction surfaces of the **a** and **a′** domains of ERp57 with Tapasin are essentially identical with those between PDI **a** and **a′** domains with MTP (Fig. 6 and *SI Appendix*, Fig. S9), with the exception of a mixed disulfide state between ERp57 and Tapasin.

Overall, the data suggest that MTPα is bound by PDI by the same sites that PDI interacts with substrate proteins during oxidative folding and hence, that MTPα can be considered a substrate mimic to study binding interactions.

Materials and Methods

Cloning. The gene encoding human MTP includes residues 19 to 894 (lacking the N-terminal signal peptide) and was amplified from a human liver complementary DNA library (Clontech). The gene was inserted into a modified pET23-based vector using NdeI/XhoI restriction site incorporating an N-terminal hexahistidine tag. The preparation of a polycistronic expression construct for codon-optimized Erv1p and codon-optimized mature human PDI (residues 18 to 509) in modified pLysS was described previously (68). Mutations in MTP were made using the QuikChange mutagenesis kit (Agilent) according to the manufacturer's instructions. All plasmids were sequenced to confirm the correct insertion of genes.

Protein Expression and Purification for Crystallization. *Escherichia coli* K-12 expression strain cotransformed with DNA plasmids containing MTP and Erv1-PDI was stored at −70 °C as a stock in 20% glycerol, streaked onto Luria broth (LB) agar plate supplemented with 100 μg/mL ampicillin and 35 μg/mL chloramphenicol, and incubated at 37 °C. This was used to inoculate 50 mL LB medium supplemented with the corresponding antibiotics, and the flask was incubated at 37 °C at 200 rpm for 6 h. This culture was used to seed 200 mL autoinduction medium supplemented with corresponding antibiotics in 2-L Erlenmeyer flasks (5.2 L in total) covered with an oxygen-permeable membrane to a final optical density at 600 nm of 0.02 and grown overnight at 30 °C shaking at 250 rpm. In the morning, protein expression was induced by the addition of Isopropyl β-D-1-thiogalactopyranoside to a final concentration of 0.25 mM, and the expression was continued for the next 24 to 26 h at 30 °C at 250 rpm. At the end of expression, cells were harvested at 3,220 × *g* for 20 min, and pellets were stored frozen at −20 °C. Cell pellets were resuspended in 200 mL of the lysis buffer (50 mM NaP, pH 7.4, 150 mM NaCl, 5 mM Imidazole) supplemented with 0.1 mg/mL lyzozyme. Cells were lysed by 2 cycles of freeze–thaw, and chromosomal DNA was broken by sonication. Cell debris was cleared out by centrifugation at 25,155 × *g* for 40 min, and supernatants were filtered through 0.45-μm syringe filters. Supernatants were loaded into 5-mL HiTrap Chelating column (GE Healthcare), which was previously equilibrated with the lysis buffer. The flow through was collected, and column was additionally washed with 50 mL of 50 mM NaP, pH 7.4, 300 mM NaCl, and 10 mM Imidazole. The proteins of interest were eluted with the step gradient of imidazole, including 20, 40, 50, and 200 mM Imidazole. All fractions were analyzed by sodium dodecyl sulfate/polyacrylamide gel electrophoresis (SDS/PAGE). Fractions containing the MTP protein complex were pooled together and concentrated to a final volume of 1.5 mL using a Millipore Amicon Stirred cell with 10-kDa cutoff membrane. Size exclusion chromatography was performed using a HiLoad Superdex S200 16/60 pg column (GE Healthcare) previously equilibrated with 50 mM BisTris Propane, pH 7.5, and 200 mM NaCl. Eluted fractions were analyzed on SDS/PAGE, and fractions containing MTP were combined and concentrated to 4 to 8 mg/mL, flash frozen in liquid nitrogen, and stored at −70 °C.

Table 2. Data collection and refinement statistics

Crystal data	MTP–PDI (PDB ID code 6I7S)
Data collection	
Space group	P1
Cell dimensions	
a, *b*, *c* (Å)	77.56, 105.6, 112.2
α, β, γ (°)	89.8, 76.9, 74.2
Resolution (Å)	49.35–2.5 (2.56–2.5)
R_{merge}	0.06 (1.39)
Mean $I/\sigma I$	8.3 (0.5)
Completeness (%)	93.8 (88)
Redundancy	1.7 (1.7)
$CC_{1/2}$ (%)*	99.8 (21)
Wilson B factor (Å^2)	74.6
Refinement	
Resolution (Å)	49.35–2.5
No. reflections	108,274
R_{work}/R_{free}	20.4/25.7
No. atoms	21,452
Protein	20,888
Ligand/ion	342
Water	222
B factors	
Protein	72.4
Ligand/ion	86.7
Water	55.6
Rmsds	
Bond lengths (Å)	0.006
Bond angles (°)	1.356

Values in parentheses are for highest-resolution shell.
*Described in ref. 85.

Small-scale production of wild-type MTP and mutants is detailed in *SI Appendix*.

Crystallization. Initial crystallization screening was performed in a 96-well format by the sitting-drop vapor diffusion method using TTP Labtech's Mosquito LCP nanodispenser and commercially available sparse-matrix crystal screens, JCSG-*plus*, Morpheus, and MIDAS (Molecular Dimensions) at 22 and 4 °C. After 2 wk, initial plate crystals of ∼5 × 20 × 50 μm were obtained in 0.1 M Tris, pH 8.5, 0.2 M Li_2SO_4, and 40% (vol/vol) PEG400 at 4 °C in a drop containing 0.1 μL of protein and 0.1 μL of crystallization solution. Optimization grid screen with varying concentration of PEG400 and pH was designed based on the initial condition but resulted in the same small crystals with no diffraction. Then, initial crystals were crushed and used for seeding into optimization grid screen with ratio of 0.1 μL of protein, 0.02 μL seeds, and 0.08 μL of crystallization solution. This procedure was repeated several times until crystals of satisfactory size and shape were obtained; however, the best crystals resulted in diffraction only up to 3.2 to 3.5 Å. Crystals were reproduced, crushed, and used as seeds in the additive screen prepared using 45 μL of modified initial crystallization condition (0.1 M Tris, pH 8.0, 0.2 M Li_2SO_4, 32% [vol/vol] PEG400) mixed with 5 μL of Additive Screen HT (Hampton Research). Crystallization experiment was set up as described before (0.1 μL of protein, 0.02 μL seeds, and 0.08 μL of crystallization solution) and incubated at 4 °C. Five days later, crystals appeared in crystallization conditions supplemented with 5% Jeffamine M-600, pH 7.0, or 4% Polypropylene glycol P400. The crystallization seeding experiment was prepared using 2 to 8% Jeffamine M-600, pH 7.0, or 2 to 8% Polypropylene glycol P425 mixed with 0.1 M Tris, pH 8.0 to 8.25, 0.2 M Li_2SO_4, and 30 to 36% (vol/vol) PEG400. Two weeks later, plate crystals of ∼10 × 100 × 100 μm appeared in 0.1 M Tris, pH 8.25, 0.2 M Li_2SO_4, 32% (vol/vol) PEG400, and 2% Polypropylene glycol P425 and were immediately flash frozen in liquid nitrogen.

Data Collection. High-resolution X-ray diffraction data were collected using MASSIF-1 (69), an automated high-throughput facility on the European Synchrotron Radiation Facility beamline ID30a-1, at a wavelength of 0.966 Å and equipped with PILATUS3_2M detector (DECTRIS); 167° of data were collected using 0.05° oscillation angle and 0.122-s exposure time. X-ray diffraction data were processed using XDS (70).

Structure Determination. CCP4 software suite (71) was used for phasing and refinement. The structure of the PDI–MTPα complex was solved by a molecular replacement (MR) method using the structures of separate domains **a**, **b**, **b**′, and **a**′ of human PDI from the Protein Data Bank (PDB) ID code 4EKZ (39) and a large β-sheet domain of lamprey lipovitellin (PDB ID code 1LSH [37]), which has 21% identity to MTPα over 65% of the length. All MR models were modified by SCULPTOR (72) to eliminate flexible and poorly conserved loops. Original attempts to position the PDI domains using MOLREP (73) were unsuccessful, and the highest rotation function peaks (higher than 6σ) were observed for the **a**′ domain. Subsequent search in Phaser (74) starting with the **a**′ domain allowed positioning of 2 copies of the **a**′ domain, 2 copies of the **b**′ domain, and a single copy of the **a** domain with log-likelihood gradient (LLG) = 621. A MOLREP search with option NP (number of peaks) = 200, where 200 rotation function peaks were used in the translation search with Phaser solution, used as a fixed model allowed positioning of a single copy of the **b** domain. Two full **a**, **b**, **b**′, and **a**′ chains of PDI were constructed by a superposition of the partial models using the **b**′ domain as a reference and subjected to rigid body refinement in Phaser (final LLG = 707) as implemented in CCP4i2 (75). REFMAC5 (76) jelly body refinement of 2 PDI monomers produced a model with R/R_{free} of 48.6/50.7.

The SCULPTOR-produced model of MTPα based on lipovitellin structure was broken into a single helical and 2 β-sheet domains. Two copies of the large β-sheet domain were positioned by the phased translation function option in Phaser (LLG = 1,020) with 2 PDI monomers used as a fixed model. This model refined to R/R_{free} values of 44/49. The refined model was subjected to 20 cycles of SHELXE phase extension procedure (77). Although the procedure did not converge, a number of long helices were built by it, which were added to the starting model. These belonged to a single α-helical MTPα domain, and MR search positioned the second copy of this domain. The 2-fold NCS (noncrystallographic symmetry) averaging implemented in DM (78) was used for phase improvement of PDI–MTPα structure, with masks and NCS operators calculated separately for each domain. Density modification phases were input for phase refinement in REFMAC5 (79). Resulting electron density maps allowed us to build the small β-sheet in both MTPα monomers in Coot (80) and to build amino acid side chains. Multicrystal averaging by DMMULTI (78) was implemented to include data collected on several nonisomorphous crystals of PDI–MTPα complex to resolution of better than 3 Å and data for several PDI structures available in the PDB. BUSTER (81) refinement was used at later stages of refinement. Model quality was assessed using MolProbity (82). For Ramachandran analysis, Ramachandran favored 95.83%, Ramachandran allowed 3.34%, and Ramachandran outliers were 0.83%. Figures were prepared in UCSF Chimera (83) and PyMol (84). Data collection and refinement statistics are presented in Table 2.

Biophysical Characterization. Protein concentration was determined by measurement of absorbance at 280 nm using molar extinction coefficients based on amino acid composition.

MTP activity was determined using the MTP activity assay kit (Roar Biochemical) according to the manufacturer's instructions except that the assay was scaled up to a 0.5- or 1-mL volume and fluorescence was monitored using a Fluoromax-4 spectrofluorometer (Horiba Scientific). The activity was measured for 15 min (semipure MTP) or 25 min (purified MTP), over which time a linear change in signal was observed. The activity assay uses an undefined fluorescently labeled lipid, making detailed interpretation of the effects of individual point mutations problematic.

Far-ultraviolet circular dichroism (CD) spectra were recorded on a Chirascan-Plus CD spectrophotometer. All scans were collected at 22 °C as an average of 3 scans using a cell with a path length of 0.05 or 0.1 cm, scan speed of 1 nm/s, step size of 1 nm, and a spectral bandwidth of 1 nm. The HT voltage did not exceed 750 V.

Thermofluor assay was performed using a 7500 Real Time PCR System (Applied Biosystems). For the assay, 22.5 μL of 0.5 mg/mL MTP in 50 mM phosphate buffer, pH 7.3, was mixed with 2.5 μL of 50× SYPRO Orange Protein Gel Stain (Sigma Aldrich) dye (original stock 5,000×, diluted to 50× before the use in 20 mM phosphate buffer, pH 7.5) and loaded onto a 96-well plate (Micro Amp reaction plate; Applied Biosystems) in 3 to 6 replicates, and the plate was sealed with a transparent film. The samples were heated from 20 °C to 90 °C, and the fluorescence signal was measured. The melting temperature (T_m) was determined by examining the derivative of the fluorescence with time.

Data Availability. Coordinates have been deposited in the PDB under ID code 6I7S.

ACKNOWLEDGMENTS. This work was supported by Academy of Finland Grants 266457 and 272573, the Sigrid Juselius Foundation, and Biocenter Oulu. We acknowledge the European Synchrotron Radiation Facility in Grenoble, France, for beamtime allocation and assistance during the X-ray data collection. The use of the facilities and expertise of the Biocenter Oulu core facilities, a member of Biocenter Finland, is acknowledged.

1. S. O. Olofsson, L. Asp, J. Borén, The assembly and secretion of apolipoprotein B-containing lipoproteins. *Curr. Opin. Lipidol.* **10**, 341–346 (1999).
2. A. Sirwi, M. M. Hussain, Lipid transfer proteins in the assembly of apoB-containing lipoproteins. *J. Lipid Res.* **59**, 1094–1102 (2018).
3. R. Lehner, J. Lian, A. D. Quiroga, Lumenal lipid metabolism: Implications for lipoprotein assembly. *Arterioscler. Thromb. Vasc. Biol.* **32**, 1087–1093 (2012).
4. S. Rustaeus, P. Stillemark, K. Lindberg, D. Gordon, S. O. Olofsson, The microsomal triglyceride transfer protein catalyzes the post-translational assembly of apolipoprotein B-100 very low density lipoprotein in McA-RH7777 cells. *J. Biol. Chem.* **273**, 5196–5203 (1998).
5. J. R. Wetterau, M. C. Lin, H. Jamil, Microsomal triglyceride transfer protein. *Biochim. Biophys. Acta* **1345**, 136–150 (1997).
6. N. O. Davidson, G. S. Shelness, APOLIPOPROTEIN B: mRNA editing, lipoprotein assembly, and presecretory degradation. *Annu. Rev. Nutr.* **20**, 169–193 (2000).
7. I. Khatun *et al*., Phospholipid transfer activity of microsomal triglyceride transfer protein produces apolipoprotein B and reduces hepatosteatosis while maintaining low plasma lipids in mice. *Hepatology* **55**, 1356–1368 (2012).
8. A. J. Hooper, F. M. van Bockxmeer, J. R. Burnett, Monogenic hypocholesterolaemic lipid disorders and apolipoprotein B metabolism. *Crit. Rev. Clin. Lab. Sci.* **42**, 515–545 (2005).
9. R. Zamel, R. Khan, R. L. Pollex, R. A. Hegele, Abetalipoproteinemia: Two case reports and literature review. *Orphanet J. Rare Dis.* **3**, 19 (2008).
10. A. J. Hooper, J. R. Burnett, Update on primary hypobetalipoproteinemia. *Curr. Atheroscler. Rep.* **16**, 423 (2014).
11. T. M. Narcisi *et al*., Mutations of the microsomal triglyceride-transfer-protein gene in abetalipoproteinemia. *Am. J. Hum. Genet.* **57**, 1298–1310 (1995).
12. E. F. Rehberg *et al*., A novel abetalipoproteinemia genotype. Identification of a missense mutation in the 97-kDa subunit of the microsomal triglyceride transfer protein that prevents complex formation with protein disulfide isomerase. *J. Biol. Chem.* **271**, 29945–29952 (1996).
13. Y. Tanaka *et al*., Structural and mutational analyses of Drp35 from Staphylococcus aureus: A possible mechanism for its lactonase activity. *J. Biol. Chem.* **282**, 5770–5780 (2007).
14. M. Di Filippo *et al*., Molecular and functional analysis of two new MTTP gene mutations in an atypical case of abetalipoproteinemia. *J. Lipid Res.* **53**, 548–555 (2012).

15. S. A. Miller *et al*., Novel missense MTTP gene mutations causing abetalipoproteinemia. *Biochim. Biophys. Acta* **1842**, 1548–1554 (2014).
16. M. T. Walsh *et al*., Novel abetalipoproteinemia missense mutation highlights the importance of the N-terminal β-barrel in microsomal triglyceride transfer protein function. *Circ Cardiovasc Genet* **8**, 677–687 (2015).
17. M. T. Walsh, E. Di Leo, I. Okur, P. Tarugi, M. M. Hussain, Structure-function analyses of microsomal triglyceride transfer protein missense mutations in abetalipoproteinemia and hypobetalipoproteinemia subjects. *Biochim. Biophys. Acta* **1861**, 1623–1633 (2016).
18. B. Ricci *et al*., A 30-amino acid truncation of the microsomal triglyceride transfer protein large subunit disrupts its interaction with protein disulfide-isomerase and causes abetalipoproteinemia. *J. Biol. Chem.* **270**, 14281–14285 (1995).
19. G. Chang, R. B. Ruggeri, H. J. Harwood Jr, Microsomal triglyceride transfer protein (MTP) inhibitors: Discovery of clinically active inhibitors using high-throughput screening and parallel synthesis paradigms. *Curr. Opin. Drug Discov. Devel.* **5**, 562–570 (2002).
20. M. T. Walsh, M. M. Hussain, Targeting microsomal triglyceride transfer protein and lipoprotein assembly to treat homozygous familial hypercholesterolemia. *Crit. Rev. Clin. Lab. Sci.* **54**, 26–48 (2017).
21. M. M. Hussain, A. Bakillah, New approaches to target microsomal triglyceride transfer protein. *Curr. Opin. Lipidol.* **19**, 572–578 (2008).
22. J. A. Wren *et al*., Efficacy and safety of dirlotapide in the management of obese dogs evaluated in two placebo-controlled, masked clinical studies in North America. *J. Vet. Pharmacol. Ther.* **30** (suppl. 1), 81–89 (2007).
23. J. R. Wetterau, D. B. Zilversmit, Purification and characterization of microsomal triglyceride and cholesteryl ester transfer protein from bovine liver microsomes. *Chem. Phys. Lipids* **38**, 205–222 (1985).
24. J. R. Wetterau, K. A. Combs, S. N. Spinner, B. J. Joiner, Protein disulfide isomerase is a component of the microsomal triglyceride transfer protein complex. *J. Biol. Chem.* **265**, 9800–9807 (1990).
25. L. Ellgaard, L. W. Ruddock, The human protein disulphide isomerase family: Substrate interactions and functional properties. *EMBO Rep.* **6**, 28–32 (2005).
26. P. Klappa, L. W. Ruddock, N. J. Darby, R. B. Freedman, The b′ domain provides the principal peptide-binding site of protein disulfide isomerase but all domains contribute to binding of misfolded proteins. *EMBO J.* **17**, 927–935 (1998).
27. J. R. Wetterau, K. A. Combs, L. R. McLean, S. N. Spinner, L. P. Aggerbeck, Protein disulfide isomerase appears necessary to maintain the catalytically active structure of the microsomal triglyceride transfer protein. *Biochemistry* **30**, 9728–9735 (1991).
28. L. J. Banaszak, W. K. Ranatunga, The assembly of apoB-containing lipoproteins: A structural biology point of view. *Ann. Med.* **40**, 253–267 (2008).
29. G. S. Shelness, A. S. Ledford, Evolution and mechanism of apolipoprotein B-containing lipoprotein assembly. *Curr. Opin. Lipidol.* **16**, 325–332 (2005).
30. M. M. W. Smolenaars, O. Madsen, K. W. Rodenburg, D. J. Van der Horst, Molecular diversity and evolution of the large lipid transfer protein superfamily. *J. Lipid Res.* **48**, 489–502 (2007).
31. J. P. Segrest, M. K. Jones, N. Dashti, N-terminal domain of apolipoprotein B has structural homology to lipovitellin and microsomal triglyceride transfer protein: A "lipid pocket" model for self-assembly of apob-containing lipoprotein particles. *J. Lipid Res.* **40**, 1401–1416 (1999).
32. C. J. Mann *et al*., The structure of vitellogenin provides a molecular model for the assembly and secretion of atherogenic lipoproteins. *J. Mol. Biol.* **285**, 391–408 (1999).
33. P. Bradbury *et al*., A common binding site on the microsomal triglyceride transfer protein for apolipoprotein B and protein disulfide isomerase. *J. Biol. Chem.* **274**, 3159–3164 (1999).
34. H. Jamil *et al*., Microsomal triglyceride transfer protein. Specificity of lipid binding and transport. *J. Biol. Chem.* **270**, 6549–6554 (1995).
35. R. Raag, K. Appelt, N. H. Xuong, L. Banaszak, Structure of the lamprey yolk lipid-protein complex lipovitellin-phosvitin at 2.8 A resolution. *J. Mol. Biol.* **200**, 553–569 (1988).
36. T. A. Anderson, D. G. Levitt, L. J. Banaszak, The structural basis of lipid interactions in lipovitellin, a soluble lipoprotein. *Structure* **6**, 895–909 (1998).
37. J. R. Thompson, L. J. Banaszak, Lipid-protein interactions in lipovitellin. *Biochemistry* **41**, 9398–9409 (2002).
38. A. Atzel, J. R. Wetterau, Identification of two classes of lipid molecule binding sites on the microsomal triglyceride transfer protein. *Biochemistry* **33**, 15382–15388 (1994).
39. C. Wang *et al*., Structural insights into the redox-regulated dynamic conformations of human protein disulfide isomerase. *Antioxid. Redox Signal.* **19**, 36–45 (2013).
40. G. Tian, S. Xiang, R. Noiva, W. J. Lennarz, H. Schindelin, The crystal structure of yeast protein disulfide isomerase suggests cooperativity between its active sites. *Cell* **124**, 61–73 (2006).
41. E. Chovancova *et al*., CAVER 3.0: A tool for the analysis of transport pathways in dynamic protein structures. *PLoS Comput. Biol.* **8**, e1002708 (2012).
42. J. R. Wetterau *et al*., Absence of microsomal triglyceride transfer protein in individuals with abetalipoproteinemia. *Science* **258**, 999–1001 (1992).
43. D. Sharp *et al*., Cloning and gene defects in microsomal triglyceride transfer protein associated with abetalipoproteinaemia. *Nature* **365**, 65–69 (1993).
44. C. C. Shoulders *et al*., Abetalipoproteinemia is caused by defects of the gene encoding the 97 kDa subunit of a microsomal triglyceride transfer protein. *Hum. Mol. Genet.* **2**, 2109–2116 (1993).
45. L. Magnolo *et al*., Novel mutations in SAR1B and MTTP genes in Tunisian children with chylomicron retention disease and abetalipoproteinemia. *Gene* **512**, 28–34 (2013).
46. M.-T. Berthier *et al*., The c.419-420insA in the MTP gene is associated with abetalipoproteinemia among French-Canadians. *Mol. Genet. Metab.* **81**, 140–143 (2004).
47. J. Wang, R. A. Hegele, Microsomal triglyceride transfer protein (MTP) gene mutations in Canadian subjects with abetalipoproteinemia. *Hum. Mutat.* **15**, 294–295 (2000).
48. M. Paquette, R. Dufour, R. A. Hegele, A. Baass, A tale of 2 cousins: An atypical and a typical case of abetalipoproteinemia. *J. Clin. Lipidol.* **10**, 1030–1034 (2016).
49. M. Gündüz *et al*., Microsomal triglyceride transfer protein gene mutations in Turkish children: A novel mutation and clinical follow up. *Indian J. Gastroenterol.* **35**, 236–241 (2016).
50. K. Ohashi *et al*., Novel mutations in the microsomal triglyceride transfer protein gene causing abetalipoproteinemia. *J. Lipid Res.* **41**, 1199–1204 (2000).
51. I. Khatun, M. T. Walsh, M. M. Hussain, Loss of both phospholipid and triglyceride transfer activities of microsomal triglyceride transfer protein in abetalipoproteinemia. *J. Lipid Res.* **54**, 1541–1549 (2013).
52. P. Rava, M. M. Hussain, Acquisition of triacylglycerol transfer activity by microsomal triglyceride transfer protein during evolution. *Biochemistry* **46**, 12263–12274 (2007).
53. P. Rava, G. K. Ojakian, G. S. Shelness, M. M. Hussain, Phospholipid transfer activity of microsomal triacylglycerol transfer protein is sufficient for the assembly and secretion of apolipoprotein B lipoproteins. *J. Biol. Chem.* **281**, 11019–11027 (2006).
54. M. Yagi-Utsumi, T. Satoh, K. Kato, Structural basis of redox-dependent substrate binding of protein disulfide isomerase. *Sci. Rep.* **5**, 13909 (2015).
55. L. W. Ruddock, R. B. Freedman, P. Klappa, Specificity in substrate binding by protein folding catalysts: Tyrosine and tryptophan residues are the recognition motifs for the binding of peptides to the pancreas-specific protein disulfide isomerase PDIp. *Protein Sci.* **9**, 758–764 (2000).
56. T. Hiroi, K. Okada, S. Imaoka, M. Osada, Y. Funae, Bisphenol A binds to protein disulfide isomerase and inhibits its enzymatic and hormone-binding activities. *Endocrinology* **147**, 2773–2780 (2006).
57. V. D. Nguyen *et al*., Alternative conformations of the x region of human protein disulphide-isomerase modulate exposure of the substrate binding b′ domain. *J. Mol. Biol.* **383**, 1144–1155 (2008).
58. B. Tsai, C. Rodighiero, W. I. Lencer, T. A. Rapoport, Protein disulfide isomerase acts as a redox-dependent chaperone to unfold cholera toxin. *Cell* **104**, 937–948 (2001).
59. M. E. Conway, C. Lee, The redox switch that regulates molecular chaperones. *Biomol. Concepts* **6**, 269–284 (2015).
60. F. Hatahet, L. W. Ruddock, Protein disulfide isomerase: A critical evaluation of its function in disulfide bond formation. *Antioxid. Redox Signal.* **11**, 2807–2850 (2009).
61. R. B. Freedman *et al*., 'Something in the way she moves': The functional significance of flexibility in the multiple roles of protein disulfide isomerase (PDI). *Biochim. Biophys. Acta. Proteins Proteomics* **1865**, 1383–1394 (2017).
62. A. Puig, H. F. Gilbert, Protein disulfide isomerase exhibits chaperone and anti-chaperone activity in the oxidative refolding of lysozyme. *J. Biol. Chem.* **269**, 7764–7771 (1994).
63. L. Wang, X. Wang, C. C. Wang, Protein disulfide-isomerase, a folding catalyst and a redox-regulated chaperone. *Free Radic. Biol. Med.* **83**, 305–313 (2015).
64. H. Lilie, S. McLaughlin, R. Freedman, J. Buchner, Influence of protein disulfide isomerase (PDI) on antibody folding in vitro. *J. Biol. Chem.* **269**, 14290–14296 (1994).
65. L. J. Byrne *et al*., Mapping of the ligand-binding site on the b′ domain of human PDI: Interaction with peptide ligands and the x-linker region. *Biochem. J.* **423**, 209–217 (2009).
66. A. Y. Denisov *et al*., Solution structure of the bb′ domains of human protein disulfide isomerase. *FEBS J.* **276**, 1440–1449 (2009).
67. G. Dong, P. A. Wearsch, D. R. Peaper, P. Cresswell, K. M. Reinisch, Insights into MHC class I peptide loading from the structure of the tapasin-ERp57 thiol oxidoreductase heterodimer. *Immunity* **30**, 21–32 (2009).
68. F. Hatahet, V. D. Nguyen, K. E. H. Salo, L. W. Ruddock, Disruption of reducing pathways is not essential for efficient disulfide bond formation in the cytoplasm of E. coli. *Microb. Cell Fact.* **9**, 67 (2010).
69. M. W. Bowler *et al*., MASSIF-1: A beamline dedicated to the fully automatic characterization and data collection from crystals of biological macromolecules. *J. Synchrotron Radiat.* **22**, 1540–1547 (2015).
70. W. Kabsch, XDS. *Acta Crystallogr. D Biol. Crystallogr.* **66**, 125–132 (2010).
71. M. D. Winn *et al*., Overview of the CCP4 suite and current developments. *Acta Crystallogr. D Biol. Crystallogr.* **67**, 235–242 (2011).
72. M. Wahle, W. Wriggers, Multi-scale visualization of molecular architecture using real-time ambient occlusion in sculptor. *PLoS Comput. Biol.* **11**, e1004516 (2015).
73. A. Vagin, A. Teplyakov, Molecular replacement with MOLREP. *Acta Crystallogr. D Biol. Crystallogr.* **66**, 22–25 (2010).
74. A. J. McCoy *et al*., Phaser crystallographic software. *J. Appl. Cryst.* **40**, 658–674 (2007).
75. L. Potterton *et al*., CCP4i2: The new graphical user interface to the CCP4 program suite. *Acta Crystallogr. D Struct. Biol.* **74**, 68–84 (2018).
76. G. N. Murshudov *et al*., REFMAC5 for the refinement of macromolecular crystal structures. *Acta Crystallogr. D Biol. Crystallogr.* **67**, 355–367 (2011).
77. A. Thorn, G. M. Sheldrick, Extending molecular-replacement solutions with SHELXE. *Acta Crystallogr. D Biol. Crystallogr.* **69**, 2251–2256 (2013).
78. K. Cowtan, Recent developments in classical density modification. *Acta Crystallogr. D Biol. Crystallogr.* **66**, 470–478 (2010).
79. N. S. Pannu, G. N. Murshudov, E. J. Dodson, R. J. Read, Incorporation of prior phase information strengthens maximum-likelihood structure refinement. *Acta. Crystallogr. D Biol. Crystallogr.* **54**, 1285–1294 (1998).
80. P. Emsley, K. Cowtan, Coot: Model-building tools for molecular graphics. *Acta. Crystallogr. D Biol. Crystallogr.* **60**, 2126–2132 (2004).
81. G. Bricogne *et al*., BUSTER (Version 2.10.3, Global Phasing Ltd., Cambridge, UK, 2018).
82. V. B. Chen *et al*., MolProbity: All-atom structure validation for macromolecular crystallography. *Acta Crystallogr. D Biol. Crystallogr.* **66**, 12–21 (2010).
83. E. F. Pettersen *et al*., UCSF Chimera–A visualization system for exploratory research and analysis. *J. Comput. Chem.* **25**, 1605–1612 (2004).
84. Schrödinger, LLC, The PyMOL Molecular Graphics System (Version 2.0, Schrödinger, LLC, New York, 2017).
85. P. A. Karplus, K. Diederichs, Linking crystallographic model and data quality. *Science* **336**, 1030–1033 (2012).